Ballistic Range Experimental Results of Radiating Wakes of Spheres at Mach 10

ROBERT B. MACDERMOTT,[1,*] NICHOLAS J. MUESCHKE,[2] NAIBO JIANG,[3] PAUL S. HSU,[4] AND SUKESH ROY[5]

[1] U.S. Air Force Institute of Technology, Wright-Patterson Air Force Base, Ohio 45433, USA
[2] Southwest Research Institute, San Antonio, TX, 78238, USA
[3,4,5] Spectral Energies, LLC, Beavercreek, Ohio 45430, USA
*robert.macdermott@us.af.mil

Abstract: Hypersonic flow field can experience significant thermochemical nonequilibrium effects. However, very little ground test data exists for nonequilibrium hypersonic wake flows. Simulating air chemistry in nonequilibrium is highly challenging due to the lack of validation data. To address a lack of validation data, ballistic free flight tests were conducted examining nonequilibrium chemistry effects in the wake of 25 mm spheres at Mach 10. A laser-based diagnostic system was used to measure naturally-produced nitric oxide concentrations. Measurements were made up to 53 body diameters behind the sphere. NO concentrations in the wake peaked between 4.1 +/- 0.8% and 6.8 +/- 1.3%.

1. Introduction

Complex aerothermodynamic phenomena dominate the hypersonic flow field, both along the body and into the wake region. At hypersonic speeds, chemical reactions, ionization, and radiation are present and, for blunt bodies, dominate the flow field along the bow shock and in the near wake region [1]. The fact that the near wake region tends to be in a nonequilibrium thermochemical state [2] complicates matters. The nonequilibrium phenomena affects both electron density and radiation. Sixty years ago Lees [1] stated that, "even for pure 'air' our understanding of the radiation from hypersonics wakes is still in a primitive state." In the intervening years, while the aerothermodynamic community's understanding has grown, Lees' statement continues to hold. Objects traveling through a fluid medium will leave a 'trail' or wake which tells of their passage. The wake region is influenced by the same nonequilibrium phenomena that are present in the near field of the object. For objects traveling a subsonic and supersonic speeds, the wake consists of primarily pressure and density variations. However, for objects traveling at sufficiently fast hypersonic speeds, the wake may contain significant temperature differences, chemically reacting flow, ionization, and radiation. The length of the wake is a temporal phenomenon which is governed by relevant localized aerodynamic, aerothermal, and chemical processes. The particles resident in the flow field, around the body and into the wake, will consist of chemical species found in the fluid and any 'contaminants' that emanate from the object's surface. For objects in Earth's atmosphere, the fluid is air, consisting of N_2, O_2, CO_2, Ar and traces of other elements. The flow field's chemical composition is dependent on local conditions and the residency time for a fluid element at the local condition. The local conditions will continue to change and evolve in the wake region.

Figure 1 shows a schematic of the shock and wake structures for a notional body flying at hypersonic speeds. As the fluid element passes the trailing edge of the object, which Lykoudis [3] defines as the corner, the flow is turned and expands isentropically [4]. As the flow moves further over the corner, the boundary layer separates from the body and continues to expand into the body's base region. Weiss [5] described the expansion of the now separated boundary layer as an essentially inviscid process. However, viscous forces remain important in the region along the dividing streamline. The dividing streamline serves as the boundary between the two distinct regions formed from the separated boundary layer; the recirculation region and the free shear layer. The dividing streamline terminates at a reattachment point [6], or in the case of a wake, at the rear stagnation point [7]. Between the free shear layer and the base of the object, a recirculation region forms. The recirculation region extends aft of the body to the rear stagnation point. At the rear stagnation point, the local fluid velocity is zero with respect to the body. Downstream from the rear stagnation point the free shear layer collapses, and a recompression shock, referred to as the trailing shock, forms. The narrowest portion of the collapsed free shear layer is known as the neck. Aft of the neck, the collapsed free shear layer is called the inner core [8]. The outer inviscid wake, which is the expanded flow from the post bow shock inviscid region, surrounds the inner core. The inviscid region, particularly for blunt bodies, will have a 'hot' inner region of high-enthalpy chemically reacting flow and a 'cool' outer region. If laminar at the neck, the viscous inner core will

eventually transition to turbulent flow. The inner core will diffuse into the inviscid wake as the flow field evolves further downstream. The point where the expanding inner core engulfs the 'hot' portion of outer inviscid wake and 'breaks' into the 'cool' regions of the inviscid wake is known as the breakthrough point [9, 10]. At this point, turbulent fluctuations provide a means for transporting cooler gases from the inviscid region into the hotter viscous core of the wake. Mixing of the cooler gases into to the viscous core can quench reduce reaction rates in the wake region and drive chemical concentrations back to a lower temperature equilibrium point. The regions between the base of the body and the neck are referred to as the 'near wake.' The region downstream of the neck is referred to as the 'far wake.'

Far wake

Near wake

Inviscid region

Bow Shock

Boundary layer

Expansion fan

Free shear layer

$M_\infty \gg 1$

Dividing streamline

Trailing shock

Transition

Diffusing inner core
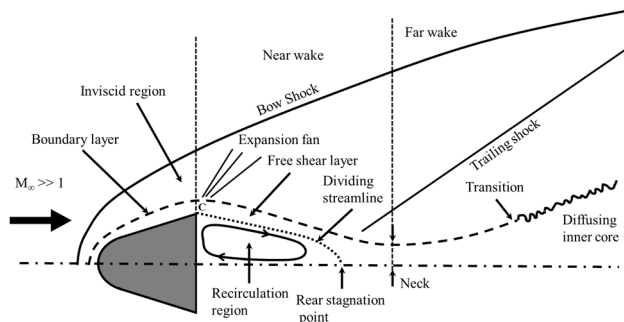
Recirculation region

Rear stagnation point

Neck

Fig. 1. Schematic representation of the different flow regions formed behind a body moving at hypersonic velocity adapted from Lykoudis [8].

The distribution of individual neutral species and ions in hypersonic wakes is influenced by the complex interplay between the total enthalpy of the flow, the body's shape, chemical kinetics, and the laminar-to-turbulent transition point of the flow [1]. A brief history of wake investigations is presented as background information.

Lykoudis provides both an abbreviated [3] and extended [8] review of hypersonic wake studies up to 1964. Lobb [11] observed nonequilibrium effects in the wakes of spheres fired from light gas guns at the United States Naval Ordinance Laboratory (NOL). Additional research at NOL observed the turbulent growths of the wakes behind spheres[12], and noted that shadowgraph technique did not observe the fluid structure of the wake prior to 200 base diameters behind the spheres.

Lyons, Brady, and Levensteins [12] investigated turbulent wake growth for sphere and cones using shadow-graphs. The primary observation on far wake structure was that the growth of the turbulent core is the same for spheres and cones at the same test conditions [12], indicating that the far wake may be insensitive to body shape, just as the scaling law proposed by Lee suggested [1]. Wilson experimentally observed the far wakes of both spheres [13] blunted cones [9] at ballistic ranges using Schlieren in 1967. The experiments observed that breakthrough, where the viscous inner core completely engulfs the outer inviscid wake, occurs further from the body for blunter bodies, in some cases over 1,000 body diameters into the wake [9].

Herrmann, Slattery, and Clay [14] observed that the far wake can continue far behind the object. Using Schlieren visualization techniques, they measured density gradients 3,200 base diameters into the far wake and faint observations as far back as 50,000 base diameters. While Wilson investigated turbulent mixing in the wake a spheres up to 10,000 body diameters into the wake [13].

Nonequilibrium effects were noted by Lobb [11] in 1964 in the wakes of spheres fired from a light gas gun. Taylor, Melcher, and Washburn [15] measured the growth of the luminous wake of spheres out to 1,200 base diameters. The wakes were asymmetric and result in elliptical cross section that are either eccentric in a constant orientation or with eccentricity that varies in a periodic manner with a period of 1 to 2 body diameters. Reis [10] measured radiation in the far wake of spheres with filtered photomultiplier radiometers which indicated NO_2 chemiluminescence, from NO + O recombination, was the dominant radiation source in the wake region. Reis [10] recorded that spheres produce long radiating wakes up to 1,600 base diameters long. Eschenroeder et al. [16] measured electron densities in free flight conditions and concluded that the neutral chemistry is frozen for between 40 to 100 base diameters behind spheres. In 1965 Stephenson [17] measured the optical radiation from the wake of blunt ablating bodies up to 30 base diameters behind the object in the NASA Ames Hypervelocity Free Flight Facility.

While state of the art at the time of the experiments, the bulk of the ballistic range hypervelocity data from the 1960s is not of sufficient quality to aid in modern computational validations. Ballistic range testing for hypersonics has dramatically slowed since the 1960s. Much of the effort from the 1970s-2010s has focused on boundary layer heating, boundary layer transition, and environmental weather effects. The current test campaign serves as an initial foray into data collection of sufficient quality to perform chemical reacting hypersonic code validation. The reported

test campaign uses modern measurement methods to investigate the concentration of NO in the flow field around and into the wake of hypersonic objects.

2. Experimental Setup

2.1 Test Facility

Experiments were conducted in the Southwest Research Institute (SwRI) large two-stage light gas gun (LGG). A two-stage light-gas gun consists of a powder breech followed by a large diameter pump tube (the first stage) followed by a high-pressure central breech with a smaller diameter launch tube (the second stage). The central breech couples the two stages. The SwRI LGG pump tube is 9.1 m long and has a 115 mm bore diameter. The launch tube is 10.4 m long and has a 38 mm bore diameter. Including the breeches, the entire gun has a length of 21.9 m. For the tests reported here, the attached environmentally-controlled flight range was 16.6 m in length. The flight range was custom configured for this test series. A mylar diaphragm was placed between the sabot stripping tank and the down range flight range. The inclusion of the mylar diaphragm allowed for the blast tank gases used to drive the sabot separation process and the test gases used for free flight study to be separated. Typical tests used N_2 in the up range region of the blast tank and a calibrated dry 79%-21% $N_2 - O_2$ mixture in the instrumented test section of the flight range.

In the first stage of the gun, a high-density polyethylene (HDPE) piston is loaded at the up-range end of the pump tube. Conventional, smokeless propellant is loaded behind it, in the main breech. Forward of the piston, the pump tube is filled with hydrogen (H_2), a low molecular weight gas (i.e., the light gas) at pressures up to 5.2 MPa. The exact powder charge and fill pressure depends upon the projectile mass and target velocity. A metal burst diaphragm is located at the down-range end of the central breech and seals the light gas in the pump tube. The diaphragm is a scored metal disc that bursts at the desired pressure. The main breech is loaded with up to 3.6 kg of smokeless propellant. The experimental projectile is loaded into the second stage of the gun near the middle breech, just down-range of the burst diaphragm.

The LGG is fired by igniting the propellant in the main breech. Propellant gases drive the HDPE piston forward, and the piston compresses the hydrogen in front of it. The metal diaphragm ruptures when the pressure at the forward end of the pump tube reaches the desired burst pressure, allowing the compressed hydrogen to flow into the launch tube and accelerate the projectile. Piston motion maintains a flow of high-pressure hydrogen from the pump tube into the launch tube. The hydrogen acts as a non-combusting compressed gas and is used as the driver gas due to its high sound speed because of its low molecular weight.

The HDPE piston decelerates and stops at the forward end of the pump tube, deforming into the tapered section of the central breech and sealing the burnt propellant gasses behind it. After the projectile exits the muzzle, the hydrogen vents into the range tankage – a series of sealed, connected pressure vessels, shown in Figure 2. New fixturing was fabricated to divide the range tankage into two sections; the sabot strip sections and the flight range section. The launch package enters the sabot section upon leaving the launch tube. The sabot separates from the projectile in flight. Inside the sabot stripping tank, the sabots impact a plate and the projectile continues into the flight range. The projectile then pierced 5 mil mylar barrier as it continued into the test gas region of the flight range. Each region of the flight range was purged before a test and then backfilled with the desired gas to the test condition pressure.
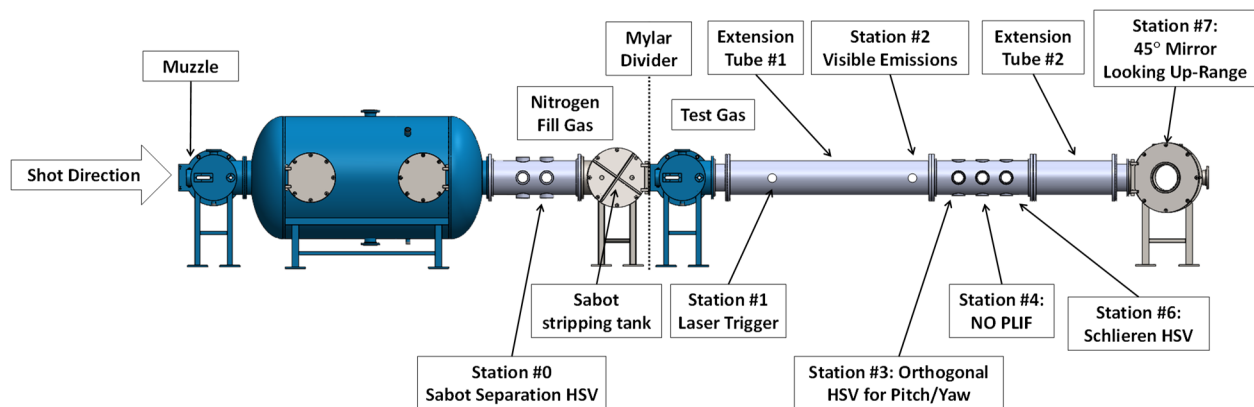

Fig. 2.   Range tankage and observation stations of the SwRI Light Gas Gun.

The test articles for these experiments were 25 mm aluminum spheres. Smaller projectiles could have been used to extend the observable region of the wake; however, a decision to use larger projectiles was made in order to maximize the imaging resolution of the new wake concentration gradients. The spheres are encased in a polycarbonate sabot, as shown in Figure 3. At total of four tests were performed during the experimental campaign. The test chamber atmospheric conditions were set to approximate Mach 10 flight at 20 km altitude. The velocity, Mach, gas composition, pressure, temperature, density, and stagnation enthalpy are shown in Table 1. Shots 498-500 were in a manufactured air mixture (79% N_2, 21% O_2), while shot 501 was a calibration shot with a known quantity of NO (98% N_2, 2% NO).

Fig. 3.   25 *mm* diameter aluminum sphere with polycarbonate sabot.

Table 1 Test conditions

LGG Shot #	Velocity *km/s*	Mach #	Gas Composition	Pressure *torr*	Temperature K	Density *Kg/m³*	$Re_{\infty,d}$	Stagnation *MJ/kg*
498	3.30	9.53	79.1% N_2 / 20.9% O_2	40	297	6.2282E-2	2.80E+5	5.45
499	3.60	10.40	79.1% N_2 / 20.9% O_2	40	297	6.2282E-2	3.06E+5	6.48
500	3.65	10.54	79.1% N_2 / 20.9% O_2	39	297	6.0725E-2	3.02E+5	6.66
501	3.52	10.02	98.0% N_2 / 2.0% O_2	40	297	6.0555E-2	3.00E+5	6.20

2.2 Optical Diagnostics

Multiple optical observations of the test shots were taken. Visible spectrum high speed imagery use used for a variety of diagnostics. Initial flash X-ray images and high speed video were used to monitor initial launch and sabot separation. One system was used to determine safes sabot separation and was located upstream of the sabot stripping tank. Two high speed cameras were located at station 3 to determine lateral and vertical position of the projectile with respect to the center line of the flight range. Imagery looking up the flight range was taken at station 6. However, the primary diagnostics were the Schlieren imagery and the Nitric Oxide (NO) Planar Laser Induced Fluorescence (PLIF) diagnostics located at stations 4 and 5. Station locations are denoted in Figure 2.

2.2.1   Schlieren

The Schlieren imagery was taken using a Phantom v2012. The Phantom v2012 is a one megapixel digital high-speed camera capable of recording from 22,000 to 1,000,000 frames per second (FPS). The frame rate is dependent on the camera's field of view. For most shots, the Phantom v2012 resolution was set to 512×256 for a frame rate of 130,000 FPS. A Z-style Schlieren configuration was used with 8 inch diameter f/10 parabolic mirrors. A pulsed diode laser operating light source was used and focused through a 400 μm pinhole.

2.2.2   NO PLIF

A burst-mode laser with a high-repetition rate compatible optical parametric oscillator (OPO) was employed for 200-kHz Nitric Oxide (NO) Planar Laser Induced Fluorescence (PLIF) diagnostics. The burst-mode OPO system was used to generate a 200-kHz rate laser pulse train at the NO Q1(38) absorption wavelength of 224.2414 nm. The 224.2414 nm wavelength was chosen as it is less sensitive to the target flow field temperature in the range of 2000 K to 4000 K. The addition of energy at the NO Q1(38) absorption wavelength resulted in NO fluorescing in the 230-300 nm A-X emission band, which was imaged using a Photron high speed camera coupled with a LaVision high speed Intensified Relay Optics (IRO) image intensifier. The intensifier gate was set to 200 ns. Two addition filters (UG11 250-400 nm band pass and a 230 nm high pass filter) were used to eliminate both laser line emissions and other hue, saturation, and value (HSV) illumination from the imaging system. The experimental setup of 200-kHz NO PLIF with Burst-mode OPO is shown in Figure 4. The PLIF system was triggered by the laser trigger located at station 2.
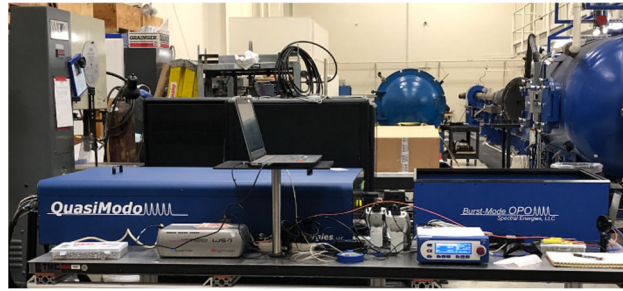

Fig. 4.   Photograph of Burst-mode OPO experimental setup at SwRI two-stage light gas-gun facility.

A continuous wave (CW) seed laser near 1064 nm was used as the oscillator for the burst-mode laser, which was equipped with seven amplifier stages to provide high pulse energy even at a repetition rate of 200 kHz. Most of the third harmonic output near 355 nm from the burst-mode laser was used to pump the OPO, which was also seeded with a CW laser at the OPO idler wavelength near 851 nm. The OPO signal generated near 609 nm was sum-frequency-mixed with the remaining 355 nm from the burst-mode laser to generate the 224 nm wavelength needed to excite nitric oxide (NO). The 224 nm laser energy was monitored using a photodiode and measured on an oscilloscope, with the laser energy estimated to be as high as 1.3 mJ/pulse at 224 nm during the relatively constant laser energy portion of the burst. The full-width-at-half-maximum (FWHM) laser linewidth at 224 nm is estimated to be approximately 0.015 cm^{-1}, nearly transform-limited laser pulses. The burst-mode laser was operated for a burst duration of approximately 1.5 ms, yielding approximately 250 laser pulses at 224 nm for a single burst when accounting for the gradual rise in the pulse energy of the laser.

The high-intensity *ns*-duration ultraviolet (UV) beam was routed into the test-section through a UV-fused silica window located on the bottom of the flight range at station 4 as shown in Figure 2. The laser sheet forming optics were used to form an approximately 76 mm long and 1 mm thickness laser sheet with approximately 30-degree angle with respect to the centerline of projectile propagation pathway. A representation of the 30-degree laser sheet is shown in Figure 5. The purpose of the 30-degree angle was to make sure that the laser sheet would cover the centerline of the projectile and wake regardless of any shot line dispersion.
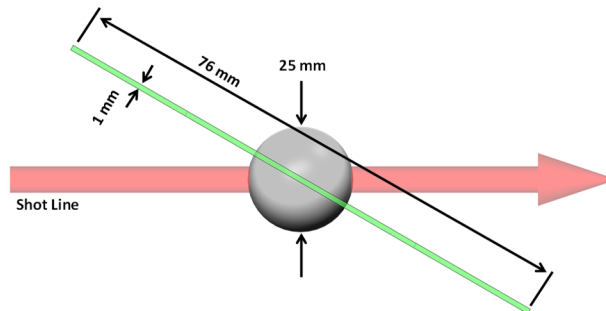

Fig. 5.   Top down view of laser sheet used for PLIF imaging.

2.3 Pre-Test Simulations

High-fidelity computational fluid dynamic simulations were used to guide the development of the test matrix. Simulations were run using the FUN3D code developed by NASA Langley Research Center [18] [19]. FUN3D is a node-based, unstructured, finite volume code that solves the conservation of mass, momentum, energy, and chemical species transport equations. Pressure is treated as an ideal gas. Temperature is determined from the total energy assuming a thermally perfect ideal gas. Transport properties are determined using NASA polynomial fits. Second order accurate HLLE++ flux reconstruction with edge-based Van Albada TVD flux limiting schemes were used for this work. A one-equation SA-Catris turbulence model was used. The baseline computational mesh was refined 10 times using the `refine` tool developed by NASA to provide additional grid resolution and align tetrahedral element edges with shocks and strong temperature gradients. An image of the starting and fully-refined computational meshes are shown in Figure 6. Version 14.0.1 of the solver was used in this work [19].
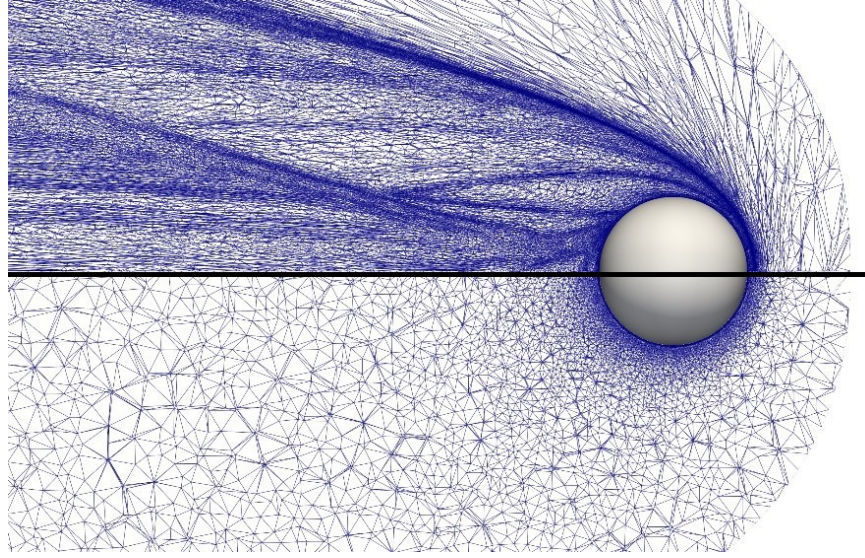

Fig. 6.   Starting computation mesh (bottom) and refined mesh after 10 refinement iterations (top).

Simulations assumed NASA's 5 species mixture for air including N_2, O_2, NO, O, and N with 5 associated chemical reactions [20]. Park's two-temperature model [21] was used to capture non-equilibrium temperature effects in the wake. Initial simulations evaluated spheres launched at Mach 8.5, 10, and 13 in freestream pressures of 10, 25, 50, 100 torr (1.3, 3.3, 6.7, and 13.3 kPa absolute). Qualitative results for the initial sphere simulations are shown in Figure 7. All simulations assumed 79% N_2 and 21% O_2 free stream conditions at 300 K. One additional simulation was run for the planned calibration test mixture of 98% N_2 and 2% NO, which is also shown in Figure 7. The images in Figure 7 show the translational-rotational temperature (T_t) and the mole fraction of NO.
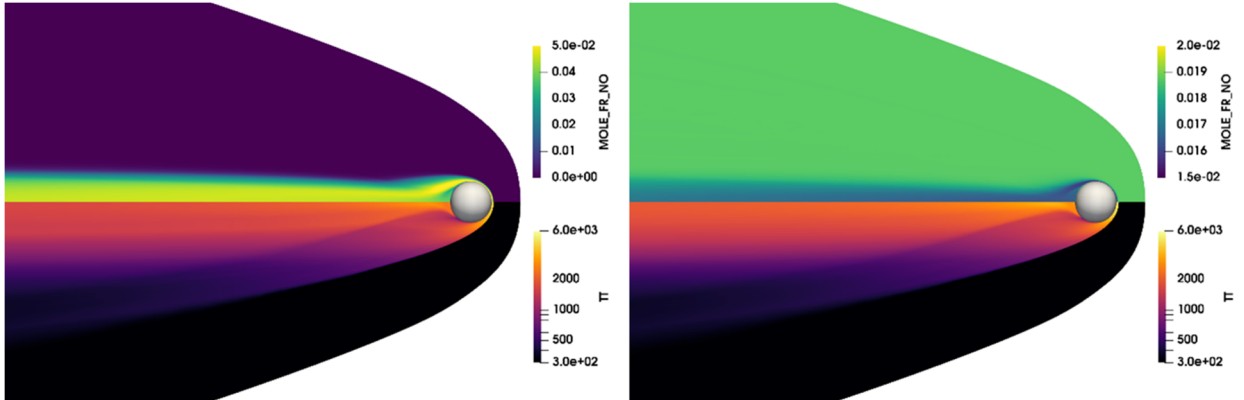

Fig. 7.   (Left) Sphere at Mach 10 in $N_2 - O_2$ freestream conditions. (Right) Sphere at Mach 10 in $N_2 - NO$ calibration gas freestream conditions.

The goal of the pre-test simulations was to estimate the shock layer and wake thermal state and resulting NO concentration. The temperature and NO concentration calculations allowed for a specific high temperature NO electronic transition to be targeted by the OPO diagnostic system. In addition, it allowed for launch velocities and flight range pressures to be set to optimize the signal return from the OPO system

2.3.1 PLIF Calibration

Care was taken in identifying the transition line selection in order to excite high temperature NO in the bow shock and wake of the projectile. Several concerns drove the selection, operation, and calibration considerations of the PLIF system. First, pre-test simulations indicated local temperatures in the wake to range from 2,000 K to 4,000 K. In air, chemical equilibrium calculations indicate that NO is generally present in the 2,000 K - 6,000 K range with peak mole fractions near 3,500 K [4]. As a consequence, the lower temperature transition frequencies of NO could not be targeted due to their insensitivity at higher temperatures. Thus, the team evaluated a range of potential transition targets from $J = 38$ to $J = 44$ of Q_{21} band, which are non-sensitive in the temperature range of interest. Table 2 show the range of transition lines and the expected relative populations of NO molecules sensitive to that transition line across a range of frequencies and temperatures. All of these transition lines have similar temperature sensitivity in the range of 2000 K – 4000 K. Ultimately, $J = 38$ transition line was selected because it provided the highest relative population of NO molecules sensitive to the target wavelength in the temperature range desired. The absorption difference with the $J = 38$ line is ~20% in the range of 2000 K – 4000 K. The predicted theoretical wavelength for this transition line is 224.2483 nm. Ultimately, the OPO was tuned to 224.2414 nm by scanning a range of frequencies around the transition point and selecting the frequency which provided the highest fluorescence signal from a hydrogen diffusion flame.

Table 2. NO absorption line strength

Temperature (K)	$J = 38$	$J = 39$	$J = 40$	$J = 41$	$J = 42$	$J = 43$	$J = 44$
2000	0.588	0.550	0.511	0.470	0.438	0.400	0.370
3000	0.568	0.550	0.521	0.500	0.500	0.460	0.440
4000	0.478	0.470	0.457	0.445	0.433	0.420	0.440

The PLIF system was designed to allow for quantitative measurements of NO mole fractions. The LIF signal recorded by the camera is given by

$$S_{LIF}(v) = \frac{C_{opt}E_pA_{(v'=0 \to v''=2)}}{[\sum_{v''} A_{v'v''} + Q(X_p,p,T_t)]}\left[\sum_i \{F_{B_i}(T_t)B_ig_i(v,X_p,p,T_t)\}\right]n_{NO} \tag{1}$$

where v is the vibration quantum state, T_t is the translational-rotational temperature, p is the pressure, X_p is species mole fraction, C_{opt} is an optical collection constant, E_p is the laser energy per pulse, A and B_i are Einstein coefficients for the emission and absorption, $f_{Bi}(T_t)$ is the equilibrium Boltzmann fraction based on the translational-rotational temperature, $Q(X_p,p,T_t)$ is the A-state quenching rate, $g_i(v,X_p,p,T_t)$ is the line shape function, and n_{NO} is the number density of NO. The number density of NO is given by

$$n_{NO} = X_{NO}\frac{p}{k_BT_t} \tag{2}$$

where X_{NO} is the NO mole fraction and k_B is the Boltzmann constant. A calibration experiment was developed to estimate these parameters. By flying through a known concentration of NO, eliminating chemical reactions with oxygen, and minimizing NO dissociation reaction, most parameters can be estimated. A gas mixture of 2% NO in nitrogen (N_2) was selected for the calibration test. With the same projectile flying conditions, the only parameters that affect the NO PLIF intensities between the calibration test and air tests are the NO concentration and the quenching rate. Here, the quenching rates between NO and main species such as N_2, O_2, and NO self-quenching are well known. Therefore, NO concentration can be calculated based on the PLIF intensities. Counting on the quenching difference

between the calibration test and the calibrated air tests, the NO PLIF signal in the calibration test is ~2.8x stronger compared to same NO concentration in real air test.

The fluorescence signals from the calibration test are shown in Figure 8. In Figure 8 d is the diameter of the sphere and x is the distance into the wake and the vertical line denotes a row of pixels at which the normalized distance into the wake (x/d) is calculated. Away from the projectile, the free stream NO behind the bow shock is visible once the bow shock heats the air to temperature sufficient to populate the $J = 8$ transition state. Combined with the temperature and pressure estimates from the simulations, the values of NO intensities can be used to analyze the NO concentrations in the tests with air in the free stream.

Taking into account the source uncertainty the quantitative mole fractions have an assessed uncertain of +/- 20%. The main sources of uncertainty are the laser energy fluctuation and the quenching effect between the calibration shot and the (LGG# 501) and the test shots (LGG #499 and #500). The laser energy fluctuations affect the energy imparted to the NO molecules and therefore the energy emitted at the targeted transition line. Laser energy fluctuations at 226 nm were estimated to be ~10%. Although the laser fluctuations at 1064 nm were less than 5%, the fluctuations were amplified by harmonics and the OPO processes. Attempts to reduce fluctuations were attempted, including heating and cooling the OPO crystals, but fluctuations in the UV wavelengths remain ~10%. The quenching effect is a function of the species density and was informed using species concentrations from the simulation. The simulations did not include time accurate diffusion of the chemical species, as the simulations must be run in a time averaged manner. The difference between the actual species concentration in the experiment and the time average concertation in the simulation continue to the uncertainty.

In addition, regions of the flow field that are outside the 2,000 – 4,000 K calibration range are not reliable. An example is the bow shock region shown in Figure 8a. The PLIF imagery of the bow shock near the stagnation point of the sphere indicates concentrations of $X_{NO} > 2\%$. In the stagnation region temperatures are expected to be approximately 5,450 K based upon CFD computations, which far exceeds the 2,000 K – 4,000 K calibration range and the NO PLIF mole fractions conversion is not valid for that region.
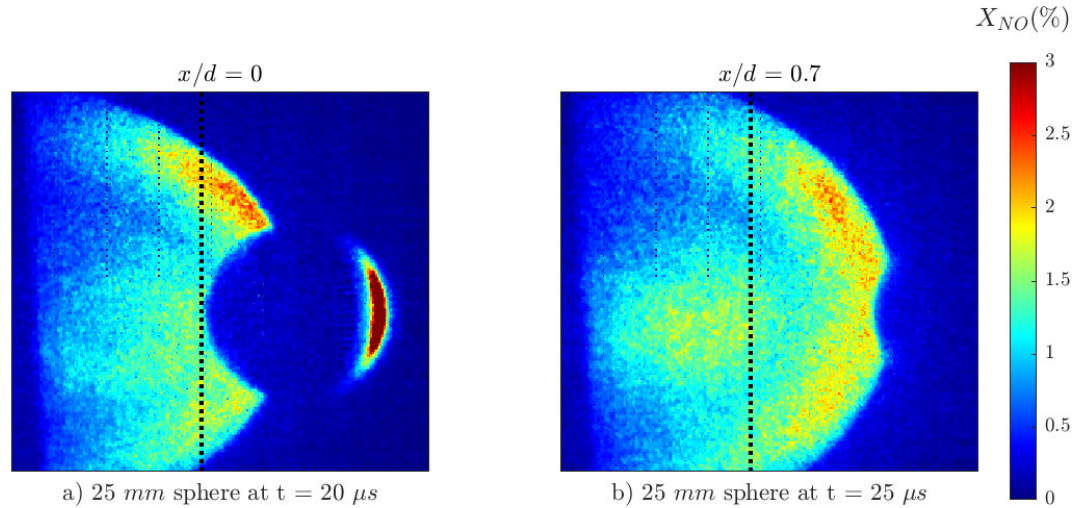

$X_{NO}(\%)$

$x/d = 0$ $x/d = 0.7$

a) 25 mm sphere at t = 20 μs b) 25 mm sphere at t = 25 μs

Fig. 8.   PLIF image of NO concentrations of the 25 mm sphere during calibration shot, LGG shot #501.

3.   Results and Discussion

The experimental results successfully observed both the fluid structures and the NO concentrations around the projectiles and into the wake. The Schlieren imagery captured the bow shock of the spheres and the onset of turbulence in the near wake. The NO PLIF measured the species concentrations of NO both spatially and temporally. A full data set was collected for LGG shots #499-501. Due to a premature triggering event, NO PLIF data was not collected on LGG shot #498. For both the Schlieren and NO PLIF imagery, $t = 0$ is defined as the high-speed imagery frame index

prior to the first observation of the sphere. The frame rate is then used to determine time index for subsequent frames. Time is rounded to the nearest microsecond.

3.1 Fluid Interactions

LGG shots #499, #500, and #501 exhibited similar fluid structural elements. Representative images of the projectile and the wake from a single LGG shot are shown in Figure 9. The bow show is clearly seen in the imagery. The test $Re_{\infty,d} \approx 3E+5$ was above the critical Reynolds number described by Lees [1] of $Re_{\infty,d} \approx 5E+4$ and therefore transition to turbulence was expected to occur in the wake. The flow appears to be laminar in the near wake region, but transitions to turbulence at the neck and can be seen in in Figure 9 a. The collapse of the free shear layer and recompression shock in the near wake are located at the neck, which is located at $x/d = 1$ in Figure 9 a. The separation between the viscous inner core and the inviscid outer sheath are clearly seen in Figure 9 b and c. At $x/d \approx 16$, Figure 9 d, the viscous inner core has expanded to fill the vertical range of the high speed camera and larger scale turbulent structures dominate the field of view. Further into the sphere's wake, between $x/d = 27$ and $x/d = 38$, there are no discernible changes in the flow field structure.
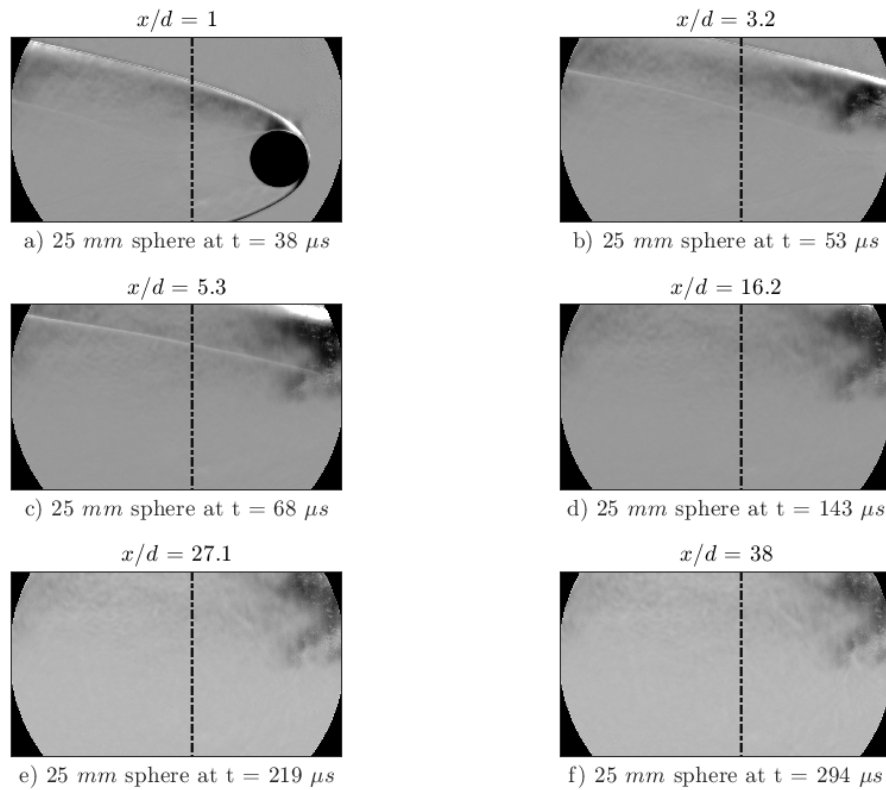
$x/d = 1$

$x/d = 3.2$

a) 25 mm sphere at t = 38 μs

b) 25 mm sphere at t = 53 μs

$x/d = 5.3$

$x/d = 16.2$

c) 25 mm sphere at t = 68 μs

d) 25 mm sphere at t = 143 μs

$x/d = 27.1$

$x/d = 38$

e) 25 mm sphere at t = 219 μs

f) 25 mm sphere at t = 294 μs

Fig. 9. Schlieren images of the near and far wake of a 25 mm sphere from LGG shot #499.

3.2 NO Concentrations

At conditions in excess of Mach 8, chemical reactions begin to take on significance and the flow field becomes a chemically reacting mixture of perfect gases [4]. The NO PLIF method used to gather data shows the species concentration of NO as they are spatially and temporally distributed across the flow field.

Results from shot #499 are shown in Figure 10. The peak NO concentrations are seen in the stagnation region, which are clearly visible in Figure 10 a-b, however, as noted previously, the mole fractions for the stagnation region are not calibrated. The near wake, where the NO PLIF calibration is appropriate, shows a centralized region of $X_{NO} \approx$ 6% in Figure 10 b-c. The X_{NO} decreases further into the wake. At $x/d = 3.5$ peak $X_{NO} \approx 5\%$ and by $x/d = 12$ peak X_{NO}

≈ 4%. These numbers are not substantially different from the CFD predictions shown in Figure 7. In the near wake and early far wake NO is homogeneous in distribution between $x/d = 12$ and $x/d = 17$, large scale structural elements begin to appear in the NO PLIF imagery and are clearly visible at $x/d = 33$. The large-scale structures indicate the presences of concentration gradients and are likely indicative of fluid structure elements, such as shed vortices. The temporal fluid structures observed within the wake are not captured by simple one- or two-equation turbulence models and highlights the need for a better understanding of wake flow physics with respect to nonequilibrium chemistry and its effects on the thermochemical state of the wake of a hypersonic object. Near the end of the test time, at $x/d = 52$, $X_{NO} \approx 2\%$.
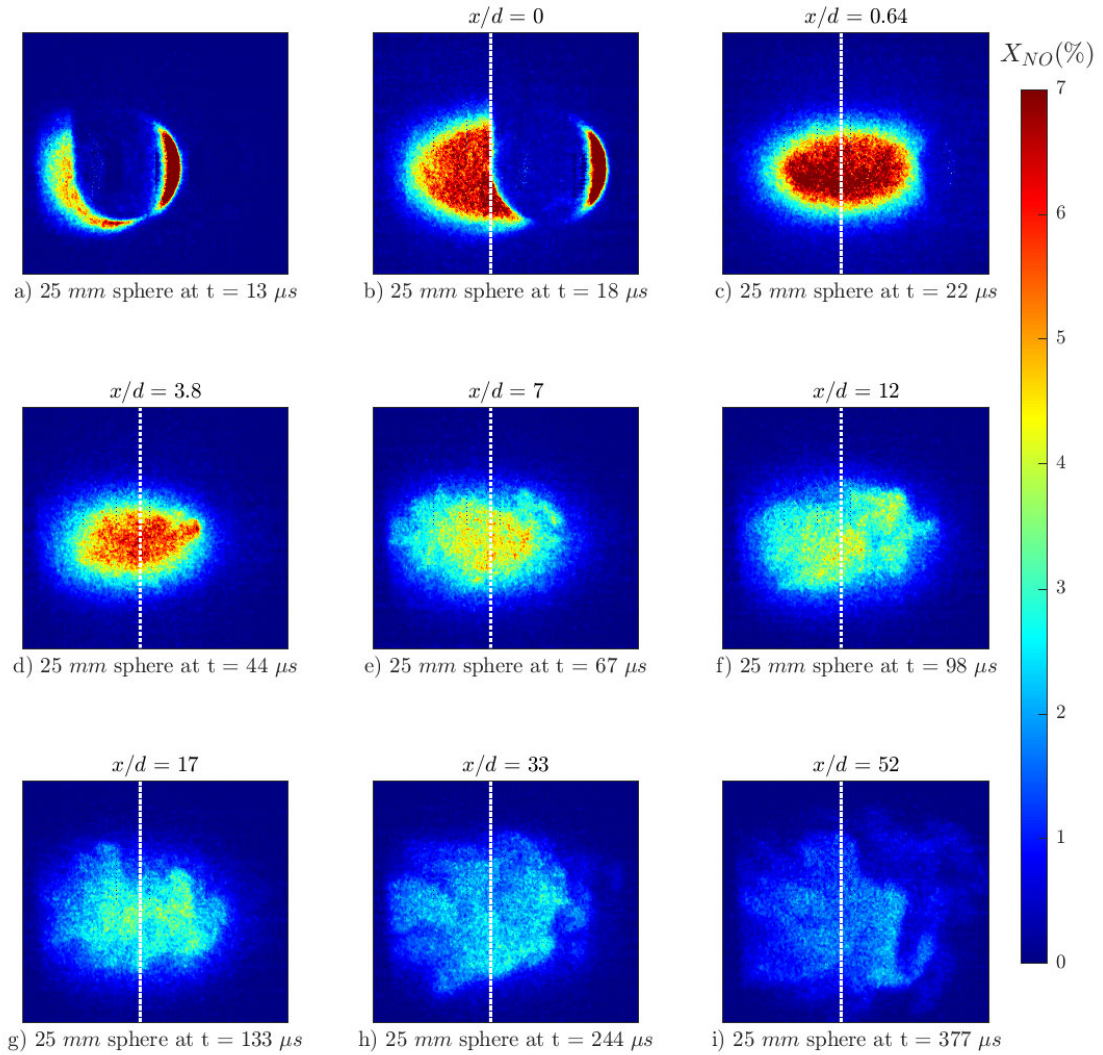

Fig. 10. PLIF image of NO concentrations of the 25 mm sphere and near wake from LGG Shot # 499.

Results from shot #500 are shown in Figure 11. The results are similar to those from shot #499. Overall the measured NO concentrations are weaker from shot #500 than for shot #499. The variation between the two shots is within the +/- 20% uncertainty bounds. The near wake in Figure 11 b-c shows a centralized region of $X_{NO} \approx 5\%$. The X_{NO} decreases from the peak near wake value. At $x/d = 4.5$ peak $X_{NO} \approx 4\%$ and by $x/d = 11$ peak $X_{NO} \approx 3\%$. The

large scale structural elements begin to emerge between $x/d = 14$ and $x/d = 21$, and are clearly visible at $x/d = 34$. Near the end of the test time, at $x/d = 53$, $X_{NO} \approx 2\%$; however, further experimentation is likely required to confirm that the local gas temperature associated with these measurements is still within the valid calibration temperature range.
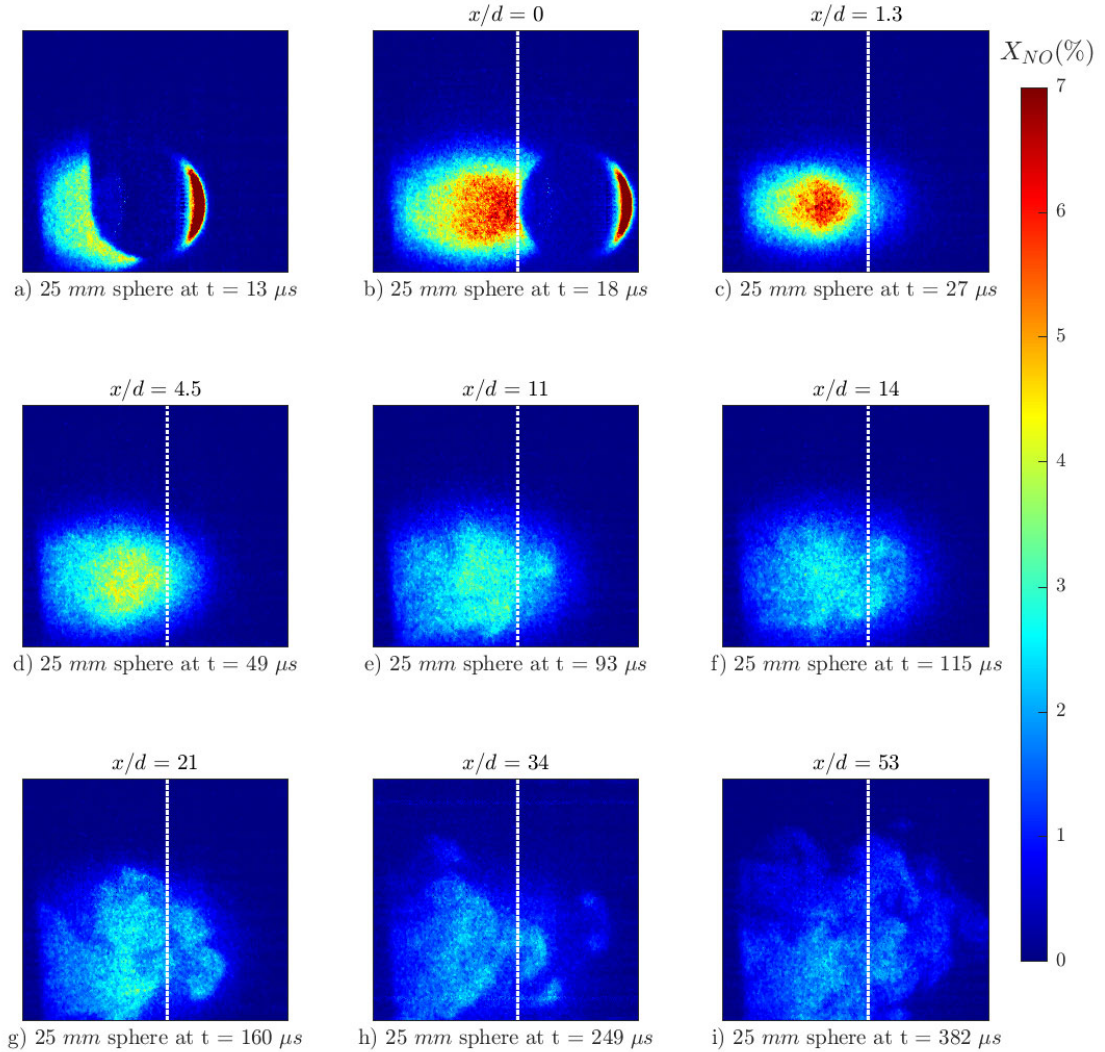

Fig. 11   PLIF image of NO concentrations of the 25 mm sphere near and far wake LGG Shot # 500.

4.   Conclusion

This paper serves to report preliminary results from the experimental test campaign undertaken at Southwest Research Institute to investigate chemically reacting hypersonic wakes. The test successfully measured the NO concentrations behind spheres traveling at Mach 10 by leveraging a novel dynamic calibration method of performing a ballistic test into a known N_2-NO mixture. Measurements were taken in three dimensions, a two dimensional plane spatially and temporally at a rate of 200 kHz. Behind the spheres, the NO concentration was observed to be homogenous in the near

wake and early far wakes. In the far wake the NO concentrations followed the bulk motion of the larger turbulent structures within the viscous core of the wake. NO concentrations were measured up to 53 base diameters in the wake.

Analysis of the test data is ongoing. In addition, post-test simulation are ongoing to determine the ability of modern computational fluid dynamics codes to accurately predict wake chemistry. Additional test campaigns and diagnostics are desired, especially diagnostics that can infer temperature of the regions of gas with measured NO concentrations. Future experimental campaigns will focus on additional velocities. The addition of a second PLIF system would enable collection of temperatures within the wake along with the species concentration.

5. Funding

6. Acknowledgement

7. Disclosures

The authors declare no conflicts of interest

8. Disclaimer

The views and conclusions contained herein are those of the authors and should not be interpreted as representing the official policies or endorsements, either expressed or implied, of Southwest Research Institute, Spectral Energies LLC, the United States Air Force, the Department of Defense, or the United States Government.

9. Data Availability

Data underlying the results presented in this paper are not publicly available at this time but may be obtained from the authors upon reasonable request.

10. References

1. Lees, L., "Hypersonic wakes and trails," *AIAA Journal*, Vol. 2, 1964, pp. 417–428. https://doi.org/10.2514/3.2356
2. Park, C., *Nonequilibrium Hypersonic Aerodynamics*, John Wiley & Sons, New York, 1990, pp. 203-206.
3. Lykoudis, P. S., "A review of hypersonic wake studies," *AIAA Journal*, Vol. 4, 1966, pp. 577–590. https://doi.org/10.2514/3.3493
4. Anderson, J. D., *Hypersonic and High-Temperature Gas Dynamics, Second Edition*, 3rd ed., AIAA Education Series, AIAA, New York, 2019, pp. 39-53,463-488. https://doi.org/10.2514/4.861956
5. Weiss, R. F., "The Near Wake of a Wedge," AVCO-Everett Research Laboratory, BSD-TDR-64-150, Research Report 197, Everett, MA, Dec. 1964.
6. Chapman, D. R., Kuehn, D. M., and Larson, H. K., "Investigation of separated flows in supersonic and subsonic streams with emphasis on the effect of transition," National Advisory Committee for Aeronautics, NACA-TR-1356, Jan. 1958.
7. Reeves, B. L., and Lees, L., "Theory of the Laminar Near Wake of Blunt Bodies in Hypersonic Flow," *AIAA 2nd Aerospace Sciences Meeting*, Vol. 24, 1965. https://doi.org/10.2514/3.3316
8. Lykoudis, P. S., "A Review of Hypersonic Wake Studies," Rand Corporation, RM-4493-ARPA, Santa Monica, CA, May 1965.
9. Wilson, L. N., "Far-Wake Behavior of Hypersonic Blunted Cones," 1967, pp. 1–7. https://doi.org/10.2514/6.1967-31.
10. Reis, V. H., "Chemiluminescent radiation from the far wake of hypersonic spheres," *AIAA Journal*, Vol. 5, 1967, pp. 1928–1933. https://doi.org/10.2514/3.4342.
11. Lobb, R. K., *Experimental Measurement of Shock Detachment Distance on Spheres Fired in Air at Hypervelocities*, 1964, pp. 519–527. https://doi.org/10.1016/B978-1-4831-9828-6.50031-X, URL https://linkinghub.elsevier.com/retrieve/pii/B9781483198286650031X.
12. Jr., W. C. L., Brady, J. J., and Levensteins, Z. J., "Hypersonic Drag, Stability, and Wake Data for Cones and Spheres," *AIAA*

Aerospace Sciences Meeting, 1964.https://doi.org/10.2514/6.1964-44

13. Wilson, L. N., "Far wake behavior of hypersonic spheres." *AIAA Journal*, Vol. 5, 1967, pp. 1238–1244. https://doi.org/10.2514/3.4177, URL https://arc.aiaa.org/doi/10.2514/3.4177

14. Herrmann, J., Slattery, R. E., and Clay, W. G., "Measured properties of the wakes of hypersonic cones," American Institute of Aeronautics and Astronautics, 1968.
https://doi.org/10.2514/6.1968-687

15. Taylor, R., Melcher, B. I., and Washburn, W., "Measurements of the Growth and Symmetry of the Luminous Hypersonic Wake Behind Blunt Bodies," *Aerospace Sciences Meeting*, 1964.
https://doi.org/10.2514/6.1964-45

16. Eschenroeder, A., Hayami, R., Primich, R., and Chen, T., "Ionization in the near wakes of spheres in hypersonic flight," American Institute of Aeronautics and Astronautics, 1966.
https://doi.org/10.2514/6.1966-55.

17. Stephenson, J. D., "Measurement of Optical Radiation from the Wake of Ablating Blunt Bodies in Flight at Speeds up to 10km per second," *NASA Technical Note*, Vol. D-2760, 1965.

18. Gnoffo, P. A., Wood, W. A., Kleb, B., Alter, S. J., Padilla, J., and White, J. A., "Functional Equivalence Acceptance Testing of FUN3D for Entry, Descent, and Landing Applications," American Institute of Aeronautics and Astronautics, 2013.
https://doi.org/10.2514/6.2013-2558.

19. Anderson, W. K., Biedron, R. T., Carlson, J.-R., Derlaga, J. M., Druyor, C. T., Gnoffo, P. A., Hammond, D. P., Jacobson, K. E., Jones, W. T., Kleb, B., Lee-Rausch, E. M., Nastac, G. C., Nielsen, E. J., Park, M. A., Rumsey, C. L., Thomas, J. L., Thompson, K. B., Walden, A. C., Wang, L., Wood, S. L., Wood, W. A., Diskin, B., Liu, Y., and Zhang, X., "NASA/TM-20220017743 FUN3D Manual: 14.0," , 2022. URL http://www.sti.nasa.gov.

20. Gupta, R. N., Yos, J. M., Thompson, R. A., and Lee, K.-P., "A Review of Reaction Rates and Thermodynamic and Transport Properties for an 11 Species Air Model for Chemical and Thermal Nonequilibrium Calculations to 30,000 K," *NASA Reference Publication*, Vol. 1232, 1990.

21. Park, C., "Assessment of two-temperature kinetic model for ionizing air," *AIAA 22nd Thermophysics Conference, 1987*, Vol. 3, 1987. https://doi.org/10.2514/6.1987-1574

22. R. MacDermott, N. Mueschke, J. Macha, S. Roy, and N. Jiang, "Laser Based Three-Dimensional Imaging of a Hypersonic Sphere's Chemically Reacting Wake," in Optica Sensing Congress 2024 (AIS, LACSEA, Sensors, QSM), Technical Digest Series (Optica Publishing Group, 2024), paper LTu1E.2.